Nano Energy 91 (2022) 106693

Contents lists available at ScienceDirect

Nano Energy

journal homepage: www.elsevier.com/locate/nanoen

Revealing Pt-seed-induced structural effects to tribological/electrical/thermoelectric modulations in two-dimensional $PtSe_2$ using scanning probe microscopy

Jong Hun Kim [a,1], Seonhye Youn [a,1], Tae Won Go [b,c], Jeongmin Kim [d], Changhyeon Yoo [e], Mashiyat Sumaiya Shawkat [e,f], Sang Sub Han [e], Seong-jae Jeon [g], Yeonwoong Jung [e,f,h,*], Jeong Young Park [b,c,**], Wooyoung Lee [a,***]

[a] Department of Materials Science and Engineering, Yonsei University, 50 Yonsei-ro, Seodaemoon-gu, Seoul 03722, Republic of Korea
[b] Department of Chemistry, Korea Advanced Institute of Science and Technology (KAIST), Daejeon 34141, Republic of Korea
[c] Center for Nanomaterials and Chemical Reactions, Institute for Basic Science (IBS), Daejeon 34141, Republic of Korea
[d] Division of Nanotechnology, DGIST, 333, Techno Jungang-daero, Hyeonpung-eup, Dalseong-gun, Daegu 42988, Republic of Korea
[e] NanoScience Technology Center, University of Central Florida, Orlando, FL 32826, USA
[f] Department of Electrical and Computer Engineering, University of Central Florida, Orlando, FL 32826, USA
[g] Department of Nano-mechanics/Nano-Convergence Manufacturing Systems Research Division, Korea Institute of Machinery and Materials, Yuseong-Gu, Daejeon 34103, Republic of Korea
[h] Department of Materials Science and Engineering, University of Central Florida, Orlando, FL 32826, USA

ARTICLE INFO

Keywords:
2D material
$PtSe_2$
Scanning probe microscopy
Friction
Metal-semiconductor transition

ABSTRACT

Two-dimensional (2D) transition metal dichalcogenides (TMDCs) provide an opportunity to investigate diverse scientific phenomena at an atomic level and have effective technological potential. In recent times, unlike conventional TMDCs, platinum diselenide ($PtSe_2$) has garnered considerable attention owing to its i) fascinating electrical and optical features coupled with mechanical strain and ii) scalable synthesis method. However, its local electrical/tribological/mechanical properties are yet to be examined in detail. In this study, we prepared two different types of $PtSe_2$ layers by controlling the thickness of the Pt-seed film: i) one with horizontal alignments, which are made from ultrathin Pt films and ii) one with vertical and horizontal alignments, which are made from a relatively thick Pt film. Then, the local tribological, mechanical, and electrical properties of $PtSe_2$ were evaluated mainly with scanning probe microscopy (SPM). The local friction study unveiled the marked friction variation depending on the layer directions. An additional study on the local mechanical property indicated that the apparent modulus difference between the two growth directions can lead to dissimilar friction behaviors. Furthermore, local current probing using SPM showed that $PtSe_2$ with both layer directions provides ohmic features to both directions, although the magnitude of conductance along the horizontal direction is ~100 times smaller than that along the vertical one. On the contrary, $PtSe_2$ with only in-plane alignments is configured with multiple horizontal $PtSe_2$ layers, densely stitching themselves together one after another with a very narrow trench region at their boundary. Surprisingly, a local current–voltage spectroscopy analysis showed a small current gap on the bridged trench region, in contrast to the ohmic behavior of the grain interior. This indicates that the local metal-to-semiconductor transition is available, owing to thin $PtSe_2$ layers in the trench regions. The following study at macroscale showed how the overall electrical and thermoelectric properties of $PtSe_2$ can be influenced by local structures triggered by the variation in Pt-seed thickness. The results not only provide a new insight on better understanding the intrinsic features of 2D $PtSe_2$, but also offer important characterization guidance on tailoring their functionalities.

* Corresponding author at: NanoScience Technology Center, University of Central Florida, Orlando, FL 32826, USA.
** Corresponding author at: Department of Chemistry, Korea Advanced Institute of Science and Technology (KAIST), Daejeon 34141, Republic of Korea.
*** Corresponding author.
E-mail addresses: Yeonwoong.Jung@ucf.edu (Y. Jung), jeongypark@kaist.ac.kr (J.Y. Park), wooyoung@yonsei.ac.kr (W. Lee).
[1] These authors contributed equally

https://doi.org/10.1016/j.nanoen.2021.106693
Received 3 August 2021; Received in revised form 14 October 2021; Accepted 2 November 2021
Available online 8 November 2021

1. Introduction

Layered materials stacked with weak van der Waals (vdW) forces have been in focus in the research community over the past two decades. Since graphene was first discovered with its unique properties in the perspective of various fields, other vdW-layered semiconductors, e.g., transition metal dichalcogenides (TMDCs), have gathered unprecedented interest owing to their fascinating electronic and physical properties [1–5]. Most studies on TMDCs has primarily focused on 6 kinds of materials with a formula of MX_2 (M=Mo, W; X = S, Se, Te) [6–8]. In contrast, apart from Mo or W-based TMDCs, Pt-based dichalcogenides had rarely been studied until the drastic bandgap shrink of $PtSe_2$, caused by the increase in thickness, was recently reported [9–11]. As the unusual behavior of the band structure can be interpreted based on the strong interlayer interaction effect, $PtSe_2$ can be suitable for the strain-engineering of an optoelectronic device [12] or a photocatalyst [13]. Moreover, a theoretical study predicted that the phonon-limited mobility of $PtSe_2$ at room temperature can be over ~4000 $cm^2/V{\cdot}s$ [14], which is ~10 times higher than that of MoS_2. From the perspective of energy, like other nanomaterials[15,16], various 2D materials have also been extensively studied, in order to improve the performances of traditional thermoelectric materials [17,18]. Although it was predicted that $PtSe_2$ should possess excellent thermoelectric properties due to its strong coupling between strain and electronic band [19,20], related experimental work is lacking [21].

Meanwhile, the synthesis of 2D $PtSe_2$ has been attempted using various approaches; a summary and comparison among these methods is presented in Table S1 of Supplementary Information. Among various synthesis methods, direct selenization of Pt-deposited substrates can form high-quality $PtSe_2$ at low temperature [11,22] on an arbitrary substrate, unlike the conventional Mo- or W-based dichalcogenide, which relies on mechanical exfoliation or high-temperature chemical vapor deposition with the transition metal oxide powder and chalcogenide gas. Besides, a facile and scalable synthesis method of $PtSe_2$ can be a great advantage in a variety of fields (i.e., electronic device, strain sensor, and thermoelectric device [22,23]). However, in spite of the such versatile attributes, several issues still remain unexplored. Particularly, chemical vapor deposition (CVD)-grown $PtSe_2$ consist of densely connected 2D-$PtSe_2$ nanograins whose individual features can be governed by their intrinsic crystallinity, and layer thickness and/or orientation [24]. Moreover, due to the strong interaction between the strain and electronic properties of $PtSe_2$ [9], a thorough understanding of local properties such as mechanical and electrical properties is required for the novel device design, which, in turn, can help tune the preparation conditions. To address the issues, local probing of a CVD-grown $PtSe_2$ at the nanoscale is a crucial step for understanding the intrinsic role of this local inhomogeneity in determining the electrical and mechanical properties of 2D-$PtSe_2$.

In this study, we studied the correlations between morphology and other electronic/tribologic/mechanical properties at the nanoscale. We prepared two different types of $PtSe_2$ samples by varying the thickness of the Pt-seed layer. First, using the friction force microscopy (FFM) study, we found that the friction anisotropy depends on the growth direction, making it feasible to distinguish the vertically standing $PtSe_2$ from the horizontal one. The following force–distance (FD) spectroscopy and quantitative peak force microscopy (QPFM) exhibited that the friction difference can be attributed to the apparent modulus difference between the crystallinity directions, which is, in turn, related to the variation of the tip-sample contact area. Next, conductive atomic force microscopy (c-AFM) combined with FFM was employed to probe the conductivity variation at the nanoscale level with regard to the growth direction and other morphological variations. We could resolve the conductivity modulation governed by the layer orientation and identified intergranular trench regions where the local metal-to-semiconductor transition occurred owing to the thinning of $PtSe_2$ layers. Such local findings can help us understand the results obtained from the macro-scaled characterization (ultraviolet photoemission spectroscopy and thermoelectric measurements) conducted at a macroscale level.

2. Experimental section

2.1. Sample preparation

Here, 2D $PtSe_2$ layers were formed on 300 nm-thick SiO_2/Si wafers using a home-built CVD system. Beforehand, Pt thin films of two different thicknesses (0.75 nm and 8 nm, respectively) were deposited on the substrate using an electron beam evaporator (Thermionics VE-100) at a rate of 0.06–0.07 Å/s. After the Pt-deposition on the SiO_2/Si substrate, Pt-deposited samples were positioned at the central heating zone of a horizontal quartz tube furnace (Lindberg/Blue M Mini-Mite), and an alumina boat with Se powder was placed inside the tube at the upstream side of the furnace. The CVD chamber was evacuated to a pressure of ~50 mTorr followed by purging with Ar gas. Subsequently, the CVD furnace was heated up to the growth temperature of ~400 ℃, which was maintained for 50 min under a constant flow of Ar gas of ~100 standard cubic centimeters per minute (SCCM). After finishing the CVD growth, we naturally cooled down the CVD furnace to room temperature.

2.2. Raman characterization

The Raman spectra were measured using a confocal Raman microscope system (LabRam Aram) at room temperature and open air. A Neodymium-doped Yttrium Aluminium Garnet (Nd:YAG) laser with wavelength of 523 nm was used, and the excitation power was set at 1 mW to minimize the surface damage. The Raman emission was collected by the same objective and dispersed with the 1800 lines/mm grating.

2.3. Transmission electron microscopy (TEM) characterization

The crystal structures of as-grown 2D $PtSe_2$ layers were analyzed using FEI Tecnai F30 TEM with an acceleration energy of 300 kV. To prepare a sample for TEM analysis, the buffered oxide etchant was applied to 2D $PtSe_2$ layers grown on SiO_2/Si substrates, and the separated 2D $PtSe_2$ layers of the SiO_2/Si substrate were mechanically scooped up to the TEM grid.

2.4. FFM and c-AFM to measure friction and conductivity

Scanning probe microscopy (SPM; Multimode 8, Bruker) was used to measure the local friction and conductivity of $PtSe_2$ layers. For FFM, a silicon tip with a nominal elastic constant of ~0.2 N/m was used in the contact mode, and the value was precisely calibrated using the thermal tune method [25]. The friction was measured by dividing the value of the lateral distortion difference between forward and backward scanning by two. For a detailed quantitative study, the measured lateral signal was converted into Newtons using the wedge method [26]. For the c-AFM study, we used a conductive Pt-coated tip with a nominal elastic constant of ~0.2 N/m. The conductive tip was directly connected to an ultra-low noise current preamplifier (gain = 10^7 V/A) to measure local current, and a voltage bias was applied to a metallic sample plate. Silver epoxy was used to make the current paths toward the metallic plate. The background current noise was smaller than ~50 fA. Lastly, for local F_n–F_f spectroscopy in FFM [27], we used Cypher AFM with the coding function (Asylum company). By coding a program, the Z-feedback was frozen, and the loading force was intentionally changed at every scan line. The motion along the slow-scan direction was fixed, so that only a single line can be repeatedly scanned. Thus, the disparity between the forward and backward lateral signals can be continually recorded during the variation in the loading force at each scan line.

2.5. Quantitative peak force microscopy (QPFM)

QPFM (multimode 8, Bruker) repetitively obtained force–distance curves whenever the cantilever was approaching/lifting at each pixel of the entire scanned area (see Fig. S1). The topography information was collected by maintaining the peak loading at each pixel. The mechanical modulation of the tip was set at 80 nm at 2 kHz. The Z-piezo travel distance was 25 nm. In the acquired force–distance curves, the reduced modulus (E^*) was estimated from the slope of the unloading curve using the following equation based on the modified Hertzian model [28]:

$$E^* = \frac{3}{4}\frac{(F_L - F_{adh})}{\sqrt{Rd^3}}, \quad (1)$$

where R, d, F_L, and F_{adh} are the tip radius, deformation, loading force, and adhesion force, respectively. The reduced modulus is given as

$$\frac{1}{E^*} = \frac{1-\upsilon_s^2}{E_s} + \frac{1-\upsilon_t^2}{E_t}, \quad (2)$$

where E_s (E_t) and ν_s (ν_t) are the elastic modulus and the Poisson's ratio of the sample (tip), respectively. ν_s and ν_t were estimated to be 0.3. To minimize the effect of the tip, a very stiff silicon tip (E_t =130 GPa, k = 40 N/m) was used. For detailed quantitative analysis, the indentation radius of the tip was calibrated by measuring the modulus of the SiO_2 substrate (~72 GPa) [29,30]. Finally, E_s was calculated from the measured E^* using Eq. (2).

2.6. Seebeck coefficient measurement

For thermoelectric measurement, rectangular-shaped $PtSe_2$ (200 × 50 μm^2) was synthesized on SiO_2/Si wafers by selectively depositing Pt-seed film on the substrate with a shadow mask. As shown in Fig. S2(a) and S2(b), the microdevice, which includes a microheater and two thermometers, was fabricated using electron beam lithography (VEGA3, Tescan Analytics). The Seebeck coefficient measurements were conducted under high vacuum conditions of $< 5 \times 10^{-6}$ Torr without convectional thermal fluctuation. The temperature difference was calibrated using the temperature coefficient of the resistance of each thermometer, which was measured by a lock-in amplifier (SR850, Stanford Research Systems) during Joule heating of the microheater. As shown in Fig. S2(c), in order to calibrate the temperature-voltage ratio for each thermometer, the measurement was performed at two different temperatures of sample base (i.e., for the 300 K measurement, T_1 = 300 K and T_2 = 303 K) The resistance of the thermometers was measured as a voltage signal by a four-probe method (each thermometer has four electrodes). Assuming a linear correlation between the thermometer signal and temperature variation, the signal value was converted into Kelvin. Finally, the Seebeck coefficient was calculated by measuring the voltage difference induced by the temperature gradient (i.e., $S = \Delta V/\Delta T$) [21,31].

3. Results and discussion

Fig. 1(a) shows the two available crystal directions of $PtSe_2$ that can be developed during the CVD growth process. In general, owing to the anisotropic bonding and surface energy minimization, vdW-layered materials prefer to form a plate-like morphology, where the exposure of active edge sites can be maximally suppressed (the top part of Fig. 1 (a)). Although a structure whose surface is entirely covered with the edge sites is also attainable by vertically arranging the 2D layers (the bottom part of Fig. 1(a)), it often becomes metastable owing to the surface energy raised by the active edges.

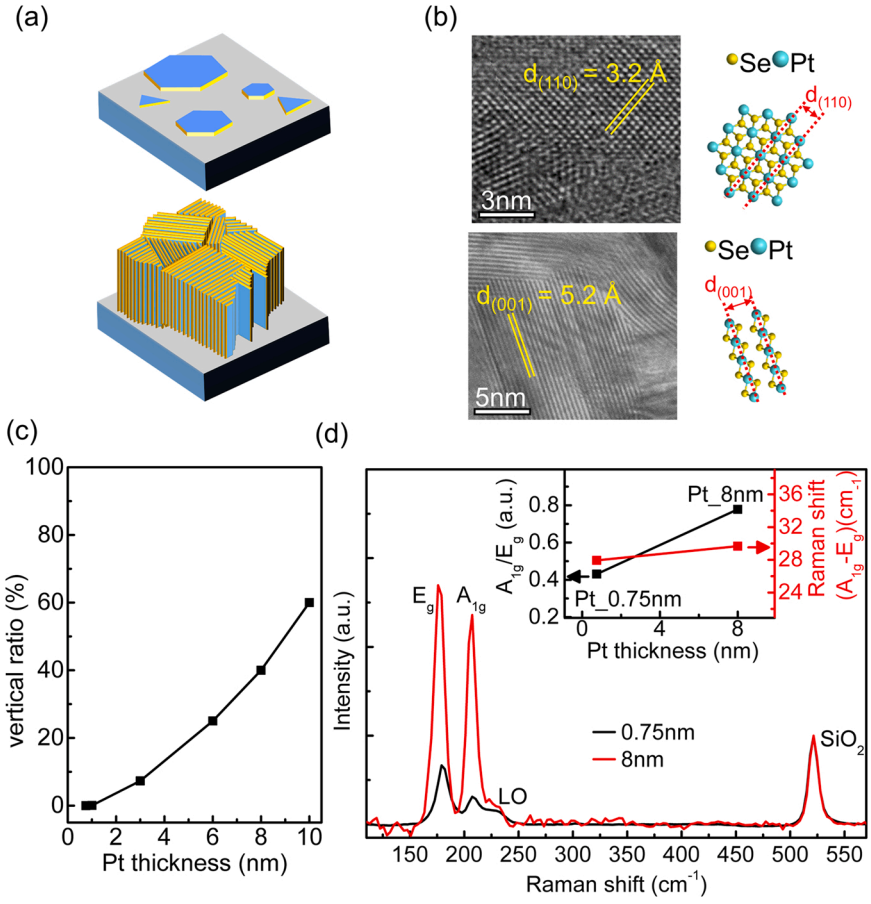

Fig. 1. (a) 2D $PtSe_2$ with two different growth directions, depending on the thickness of Pt-seed layer; (top) horizontally aligned $PtSe_2$ nanoplates produced from ultrathin Pt nano-islands; (bottom) $PtSe_2$ perpendicularly aligned to the substrate, which is produced by thick Pt films. (b) TEM images of the horizontally aligned 2D $PtSe_2$ layers (top) prepared with Pt of 0.75 nm and vertically aligned 2D $PtSe_2$ (bottom) prepared with Pt of 8 nm. They are denoted as Pt_0.75 nm and Pt_8nm. (c) Coverage ratio of vertically aligned 2D PtSe2 layers as a function of Pt thickness (d) Raman spectroscopy results of 2D $PtSe_2$ samples produced from Pt-seed film of two different thicknesses (Pt_0.75 nm and Pt_8nm); (inset) the intensity ratio and Raman shift difference between Pt_0.75 nm and Pt_8nm.

However, in this study, we developed two distinct types of 2D-$PtSe_2$: (i) $PtSe_2$ synthesized with a 0.75-nm-thick Pt-seed layer (referred to as Pt_0.75 nm hereinafter) and (ii) $PtSe_2$ with 8-nm-thick Pt-seed layer (referred to as Pt_8nm hereinafter), thereby overcoming the surface energy issue with regard to the recent research result [22]. Subsequently, their crystal structures were confirmed using TEM. The top part of Fig. 1(b) shows a typical TEM image of Pt_0.75 nm. The contrast section displays heavy Pt atoms in $PtSe_2$ because the TEM intensity scales with the atomic mass of elements. The TEM image of Pt_0.75 nm resolved the configuration of Pt with a spacing of 0.32 nm. As illustrated, the value is well-matched with the (110) planes, indicative of a top view of $PtSe_2$ along the c-axis. Combined with their polycrystalline structures observed through low-magnification TEM, we can confirm that Pt_0.75 nm is made up of horizontal $PtSe_2$ elements at different azimuthal rotation angles. However, as indicated with the red arrows in the large-scale image (Fig. S3), the TEM image of Pt_8nm displays different patterns, apart from the top-view patterns. The area indicated by the arrows was magnified (bottom part of Fig. 1(b)). In the TEM image, the layers of $PtSe_2$ were well resolved along the thickness direction, and the spacing between the layers was measured to be ~5.2 Å, which was consistent with the interlayer spacing of $PtSe_2$ along the (001) direction. Thus, we could synthesize two different types of 2D-$PtSe_2$: 1) Pt_0.75 nm (horizontal alignments) and 2) Pt_8nm (vertical and horizontal alignments). Additionally, in order to clarify the effect of thickness of Pt seed on the growth direction of $PtSe_2$, the surface structure of $PtSe_2$ layers grown from Pt with various thickness was systemically inspected by TEM and SAED (selective area electron diffraction). As a result of Fig. S4, the areal coverage ratio of vertically aligned 2D $PtSe_2$ layers was estimated from TEM images of each sample, and the result was plotted in Fig. 1(c). Fig. 1(c) exhibits a clear trend that the preferable crystal alignment of $PtSe_2$ layers pivoted from a horizontal direction to a vertical one with increasing layer thickness of Pt seed. The vertical ratio of $PtSe_2$ grown from 1 nm-Pt was estimated to be as small as ~0.5%. The results are consistent with Fig. 1(b) and in agreement with the previous result [22].

The phonon properties of Pt_0.75 nm and Pt_8nm were characterized by Raman spectroscopy. We found that the signal intensity of $PtSe_2$ relative to Si mode (~520 cm^{-1}) increased with the increase in the thickness of the Pt-seed layer. That can be attributed to the thicker coverage of Pt_8nm rather than Pt_0.75 nm. After the overall Raman curves were normalized to the intensity of Si, two Raman spectra were displayed in Fig. 1(d). As shown in the figure, two characteristic Raman modes were detected. $A_{1\,g}$ (~179 cm^{-1}) and E_g (~207 cm^{-1}) correspond to the in-plane and out-of-plane vibration motions of top and bottom Se atoms inside an atomic layer, respectively. A longitudinal optical (LO) peak attributed to the overlap of the in-plane (E_u) and out-of-plane ($A_{2\,u}$) modes was weakly detected at ~235 cm^{-1} as well. The inset of Fig. 1(c) shows that the $A_{1\,g}/E_g$ intensity ratio of Pt_0.75 nm increases with an increase in the thickness of Pt seed (in black). The results qualitatively agree with those of previous studies [22,32]. However, the Raman spectroscopy study failed to examine any spatially resolved Raman features of Pt_8nm with two pronounced growth direction differences. This can be attributed to the limited spatial resolution of Raman analysis as compared to the polycrystalline structure with a size of several tens of nanometers.

Then, we characterized the tribological properties of two $PtSe_2$ films using the FFM mode of SPM. Using a silicon cantilever, the half value of lateral deflection difference between the two scanned directions was considered as friction. For quantitative analysis, the calibration of the elastic constant and lateral diffraction of the tip was conducted beforehand [25,26]. Fig. 2(a) shows the large-scaled topography with the corresponding friction distributions for both samples. The scanning area was 1 × 1 μm^2, and the loading force, and a scan rate were set at 4 nN and 1 Hz, respectively; the loading conditions were gentle so that neither tip wear nor sample surface scratches were detected. Some contaminants were observed on the surface. However, as they could be easily swept out by repetitive scanning while keeping the rest region intact (Fig. S5), they were disregarded in the analysis. As shown in Fig. 2 (a), the average roughness of the Pt_0.75 nm topography was ~0.3 nm, indicating a smooth polycrystalline structure. Accordingly, a

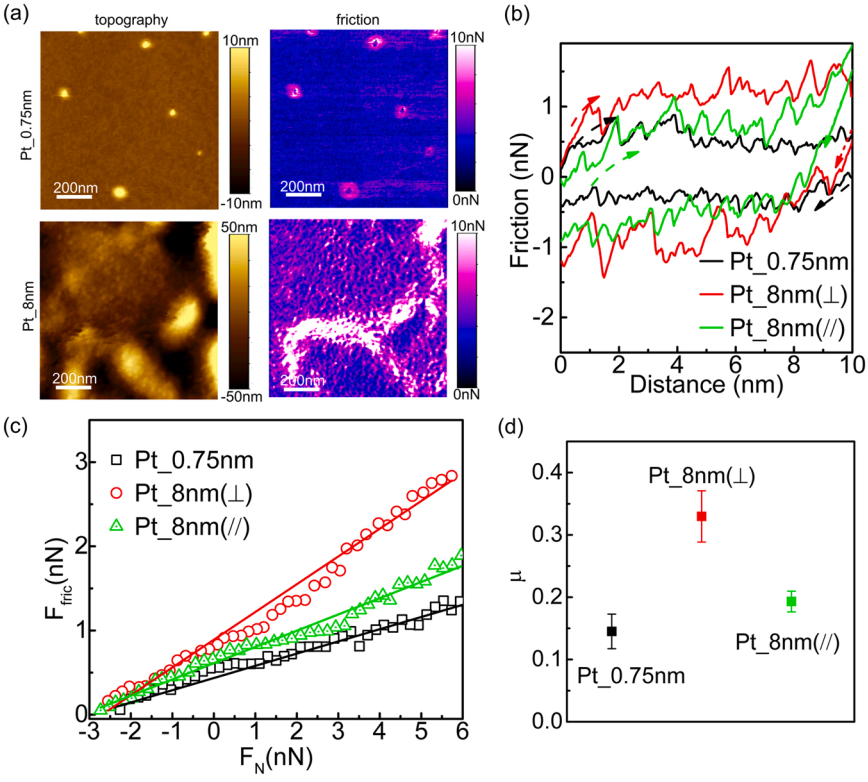

Fig. 2. (a) SPM topography (left) and friction (right) images obtained for the 2D $PtSe_2$ produced from Pt-seed films with two different thickness (0.75 (top) and 8 nm (bottom)). (b) Friction loop obtained in three different regions (Pt_0.75 nm, Pt_8nm(//), and Pt_8nm(⊥)). (c) Representative local load-friction spectroscopy results obtained for Pt_0.75 nm, Pt_8nm(//), and Pt_8nm(⊥)). The fitting lines based on the linear model were plotted together using the same color code. (d) Friction coefficients of Pt_0.75 nm, Pt_8nm(//), and Pt_8nm(⊥)).

homogeneously low friction distribution of ~3 nN was measured over the entire area. On the contrary, Pt_8nm exhibited some areas that became crumpled with a height of a few tens of nanometers above the surface in the topography; moreover, the corresponding friction increased remarkably by tens of nN. On the other hand, the remaining area still remained almost flat, keeping relatively smooth roughness (~0.9 nm) and low friction (~4 to ~5 nN). With regard to the large scanned area of Pt_8nm (Fig. S6(a)), the high-friction region was estimated to cover ~45% of the entire area. The value is close to the previously reported coverage ratio of vertical $PtSe_2$ of Pt_8nm [22]. Thus, we concluded that the protruded regions with high friction, observable only in Pt_8nm, can be attributed to the vertical $PtSe_2$, while the flat regions with low friction observed in both samples represent the horizontal $PtSe_2$ layers. The corrugated morphology can be understood with respect to total energy minimization. When the Pt seed is extremely thin (i.e., 0.75-nm Pt in our study), it is preferable to suppress the generation of active edge areas at the cost of selenization-induced strain energy to reduce the overall energy. However, the balancing trend can be altered for the thick Pt-seed layer (i.e., 8-nm Pt), where the gain of strain energy overwhelms a loss of surface energy, allowing vertical growth. Once vertical growth becomes allowable, the growth rate can significantly increase owing to the intrinsic growth attribute of vdW-layered materials; the intralayer diffusion is preferable to the growth-crossing vdW space. As a result, the crumpled regions of Pt_8nm accommodate bunches of vertical $PtSe_2$ layers with various vertical lengths, which eventually aggravates the surface smoothness and also makes it difficult to explore the intrinsic friction properties of $PtSe_2$. Therefore, the growth pattern can be somewhat tuned by changing the accumulation degree of strain energy through CVD growth parameters [33], templates [34], or e-beam irradiation [35], etc. To examine the intrinsic tribological properties, we inspected the inside of a single $PtSe_2$ grain with a scan size of 10 nm at 1 Hz (Fig. S6(b)), avoiding the grain edges. The representative friction loops of Fig. 2(b) visualized the intrinsic friction trend of Pt_0.75 nm and horizontal and vertical regions of Pt_8nm (denoted as Pt_8nm(//), and Pt_8nm(⊥), respectively). The half-height and enclosed area of the loop can be interpreted as the friction and dissipated energy occurring during the friction process, respectively. While Pt_8nm(⊥) shows the widest loop (the highest friction), Pt_0.75 nm exhibits the narrowest shape (the lowest friction). Meanwhile, Pt_8nm(//) exhibited a little broadening compared with Pt_0.75 nm, thereby indicating that their friction difference is marginally small. Accordingly, the dissipated energy values were estimated to be 18×10^{-18}, 8×10^{-18}, and 11×10^{-18} J for Pt_8nm(⊥), Pt_0.75 nm, and Pt_8nm(//), respectively. The tribological difference among the three regions can be verified more evidently based on normal load vs. friction (F_n–F_f) spectroscopy results (Fig. 2(c)). To exclude the grain edge effect, a 10-nm single line inside a single grain was continuously scanned to obtain the F_n–F_f spectroscopy results at a few different positions for each case. As shown in the representative F_n–F_f curves of Fig. 2(c), the linear friction behaviors typically appeared, regardless of sample type or scan position. Such linear dependence between friction and loading force is associated with multi-asperity contact, where the elastic deformation is prevalently considerable [27,36,37]. Therefore, we could fit the measured F_n–F_f curves to the following equation:

$$F_f = \mu(F_n - F_0), \tag{3}$$

where μ is the friction coefficient and F_0 is the adhesion force, which is determined at zero friction force. The average friction coefficients, obtained from different positions, are presented in Fig. 2(d). Each error bar indicates the standard deviation value. As shown in Fig. 2(d), the friction coefficients of Pt_0.75 nm, Pt_8nm(⊥), and Pt_8nm(//) were ~0.15, ~0.32, and ~0.19, respectively, validating the trend of the previous friction loop analysis. Compared to Pt_8nm(//), the highest μ, the difference between Pt_0.75 nm and Pt_8nm(//) was relatively small. The small difference between two horizontal $PtSe_2$ can be qualitatively understood as the 2D-multiple spring model[38] where the total lateral stiffness is reciprocally proportional to the layer number. Therefore, thickness-dependent friction difference is rapidly enhanced only when the layer number decreases to mono-or few-layers; otherwise, the declining rate of friction will be pretty mild for the decreasing number of layers. On the other hand, the adhesion force was measured to be as small as ~3 nN for the three regions. Since the surface energy is more directly proportional to the adhesion rather than friction coefficient [39–41], the trends discrepancy between adhesion force and friction coefficient implies that the contribution of the surface energy to the total friction seems to be insignificant in our FFM test condition. Pretty often, as the moisture in the ambient condition or the surface oxygen tends to significantly increase the adhesion force [37,42], the oxidation-resistant attribute [23] of $PtSe_2$ is considered to keep the adhesion force at a sufficiently low level. As depicted by the X-ray photoelectron spectroscopy (XPS) data of Fig. S7, the entire Pt 4*f* spectra can be assigned to Pt^{4+}, corresponding to $PtSe_2$ for both samples, without any oxidation-related states in the Pt4*f* spectra (Fig. S7(a) and (b)). Moreover, based on the XPS spectra, the chemical ratio of Pt/Se of both samples was estimated as ~53% (Fig. S7(c)). Therefore, we could confirm that the $PtSe_2$ samples exhibited the stoichiometric coordination at the atomic level without the oxidation effect [22,43]. Additionally, such poor adhesion difference could be partially associated with small loading force and small tip radius regime like in the conditions of our FFM test [41].

Furthermore, to qualitatively establish the reason for a regional frictional difference, FD-curve spectroscopy was conducted over the corresponding regions of Pt_0.75 nm, Pt_8nm(//), and Pt_8nm(⊥), respectively. Based on the complete trace of the FD curve (Fig. S8), we magnified the contact/retract regimes as shown in Fig. 3(a), where the slope of the curve increased in the order of Pt_0.75 nm > Pt_8nm(//) > Pt_8nm(⊥). Moreover, the hysteresis area caused by the discrepancy between the contact/retract processes increases in the same order. Fig. 3 (b) and (c) present the slope values of the tangential region and integration values of the hysteresis area, respectively, for Pt_0.75 nm, Pt_8nm(//), and Pt_8nm(⊥). As shown in the figures, the slope and hysteresis area were assessed in the same increasing order as that of friction. Additionally, the adhesion force magnitude of Pt_0.75 nm, Pt_8nm(⊥), and Pt_8nm(//) is similar enough to imply that the surface energy made only a minor contribution to friction in the small loading force regime of ~10 nN, like FFM test conditions. Thus, we assumed that the observed friction variation might have been dominated by the modulus-induced contact area difference [44,45] between the tip and sample, which would result in more energy dissipation and higher friction. Since Pt_8nm(⊥) possesses more vdW spaces on its surface, tip-induced surface deformation could be greater than others.

To validate our hypothesis, a more quantitative and statistical characterization of mechanical properties was conducted with QPFM, where FD spectroscopy analysis was conducted at every scan point. Based on Fig. S1, adhesion force, energy dissipation, and deformation values were determined. The modulus value of the sample can be extracted from the slope of the FD curve using Eqs. (2) and (3). Specifically, to minimize the effect of the tip, a stiff Si tip was used, and its contact radius was precisely calibrated in reference to the modulus of SiO_2 [29,30], which allowed the modulus to be quantitatively analyzed. Fig. 3(d) shows the spatial distributions of the topography, adhesion force, energy dissipation, modulus, and deformation of $PtSe_2$, which evolved with the thickness of the Pt-seed layer. The corresponding signal distributions are plotted in Fig. S9. The QPFM results for Pt_0.75 nm (the upper row images) reveal the homogeneous distributions of high modulus, low deformation, low energy dissipation, and low adhesion force over the entire surface. However, in the case of Pt_8nm, the spatial correlations of mechanical parameters with the corresponding topography were observed. In other words, for Pt_8nm(⊥) (high region as per topography), we identified a low modulus, high deformation, and high energy dissipation with a slight increase in adhesion. However, for

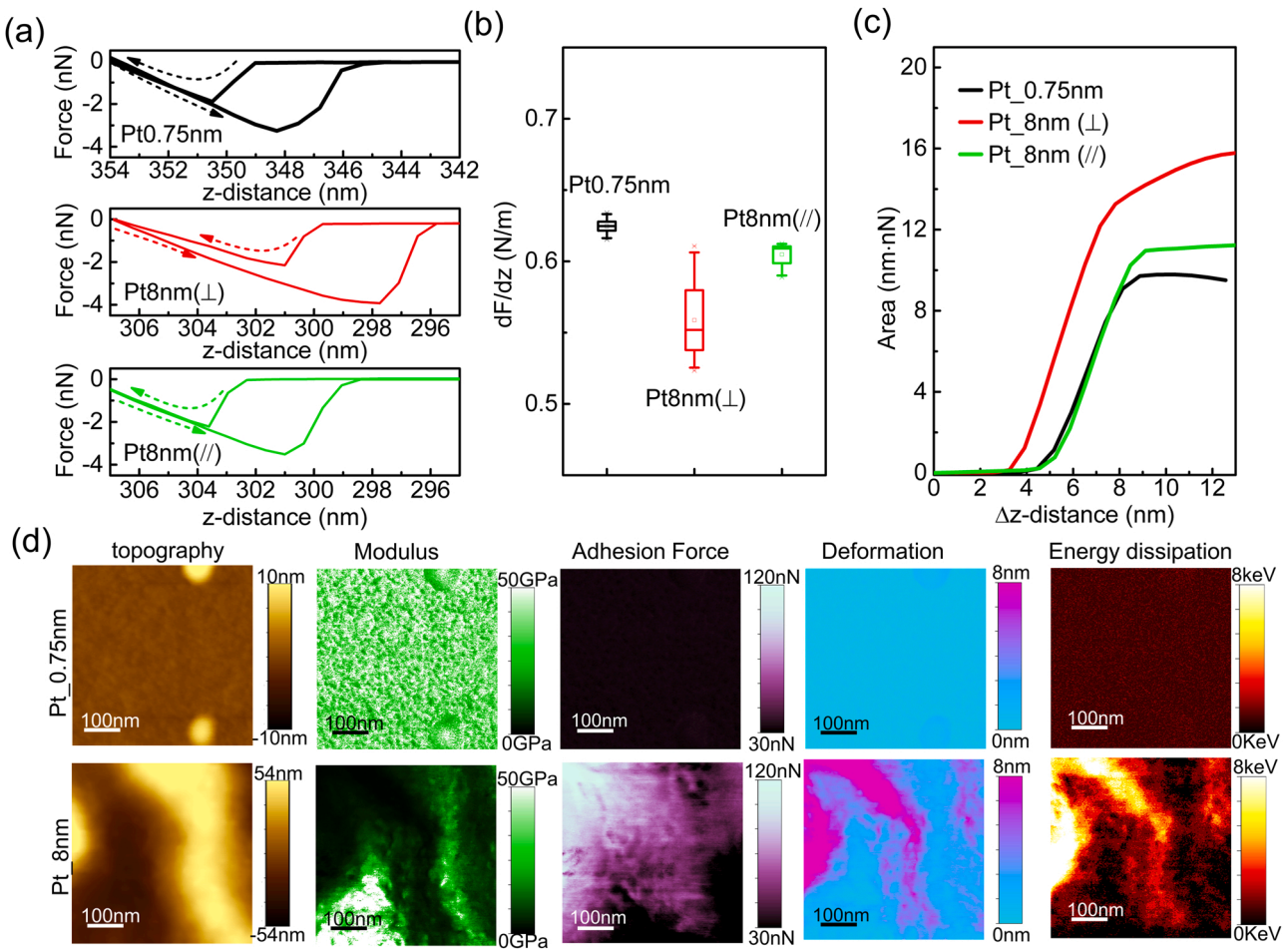

Fig. 3. (a) F–D curves measured on (top) Pt_0.75 nm, (middle) Pt_8nm(⊥), and (bottom) Pt_8nm(//), respectively. Specifically, the contact/retract regimes were magnified from Fig. S9. The arrows indicate the direction of the SPM probe movement. (b) Force slopes of the F-D curve during the loading process. (c) Integration of force difference between the loading and unloading processes with respect to the travel distance of probe, which corresponds to the dissipated energy. (d) QPFM images acquired for (top) Pt_0.75 nm and (bottom) Pt_8nm.

Pt_8nm(//) (low region as per topography), the opposite trends were observed in the mechanical parameters. As a result, we found that the overall distribution of Pt_8nm was more dispersed than that of Pt_0.75 nm (Fig. S9). Thus, we verified our hypothesis about the origin of the friction differences by revealing the relationship between the mechanical properties and friction. As friction is proportional to the contact area at the nanoscale [36,46], the lower modulus of the sample leads to a larger contact area, which increases the deformation and energy dissipation. However, a larger modulus can induce a smaller contact area, which results in lower deformation and lower energy dissipation. As mentioned earlier, we found that coupling with adhesion was present but not strong. This can be attributed to both the oxidation -resistant surface of $PtSe_2$ and the magnitude of loading force. However, the site-dependent adhesion difference became observable in a QPFM study, owing to the high loading force regime ($F_L <$ ~100 nN). The relatively greater increase in the adhesion force was of Pt_8nm(⊥) may be related to the more exposed active edge sites with lower modulus than the other regions. In addition, we considered a competing effect (called the "puckering effect"). If the puckering effect becomes dominant, more significant friction should be observed in Pt_0.75 nm than in Pt_8nm. However, the puckering effect has been reported on the exfoliated vdW-layered material weakly attached to the substrate [47], which is not similar to the directly synthesized case as in this study [48]. Thus, the puckering-induced contact area difference was precluded in our samples.

Next, the electrical property of $PtSe_2$ was investigated. In advance, ultraviolet photoemission spectroscopy (UPS) was performed to identify the surface electrical properties at macroscale. The energy region near the Fermi level (E_F defined at 0 V) was suggested as shown in Fig. 4(a). The valence band maximum (VBM) was estimated from the onset energy determined based on linear extrapolation (magenta-dashed lines). As shown in Fig. 4(a), there existed a small gap of ~0.1 V between the VBM and the E_F on the surface of Pt_0.75 nm, reflecting the semiconducting property. However, for Pt_8nm, the VBM exhibited an up-shift making it equivalent to E_F, indicative of the metallic property. Our results agree with those of a previous transistor-based study, suggesting the availability of semiconductor-to-metal transition in CVD-grown $PtSe_2$ with the increasing thickness of the Pt-seed film [22]. However, the previous study ambiguously speculated over the transition phenomena, owing to the absence of local characterization. Therefore, c-AFM combined with FFM was employed to investigate the local electrical conductivity of 2D $PtSe_2$ films. Fig. 4(b) exhibits 1 μm× 1 μm-scaled topography/friction/current images under the sample bias (V_S) of −0.1 V. The FFM study made it easy to discern the differences among Pt_0.75 nm, Pt_8nm(//), and Pt_8nm(⊥). The entire surface area was observed to be configured with tiny current spots with good uniformity on Pt_0.75 nm. The current magnitude of the spots was as small as ~2 nA. However, on Pt_8nm, a more coarsened spatial distribution was observed in the current image, and the measured current scale was significantly expanded to over a few hundred nanoamperes. Based on the FFM image of Fig. 4(b), it is clear that such high-conductance regions correspond to vertical $PtSe_2$, while the low-conductance regions

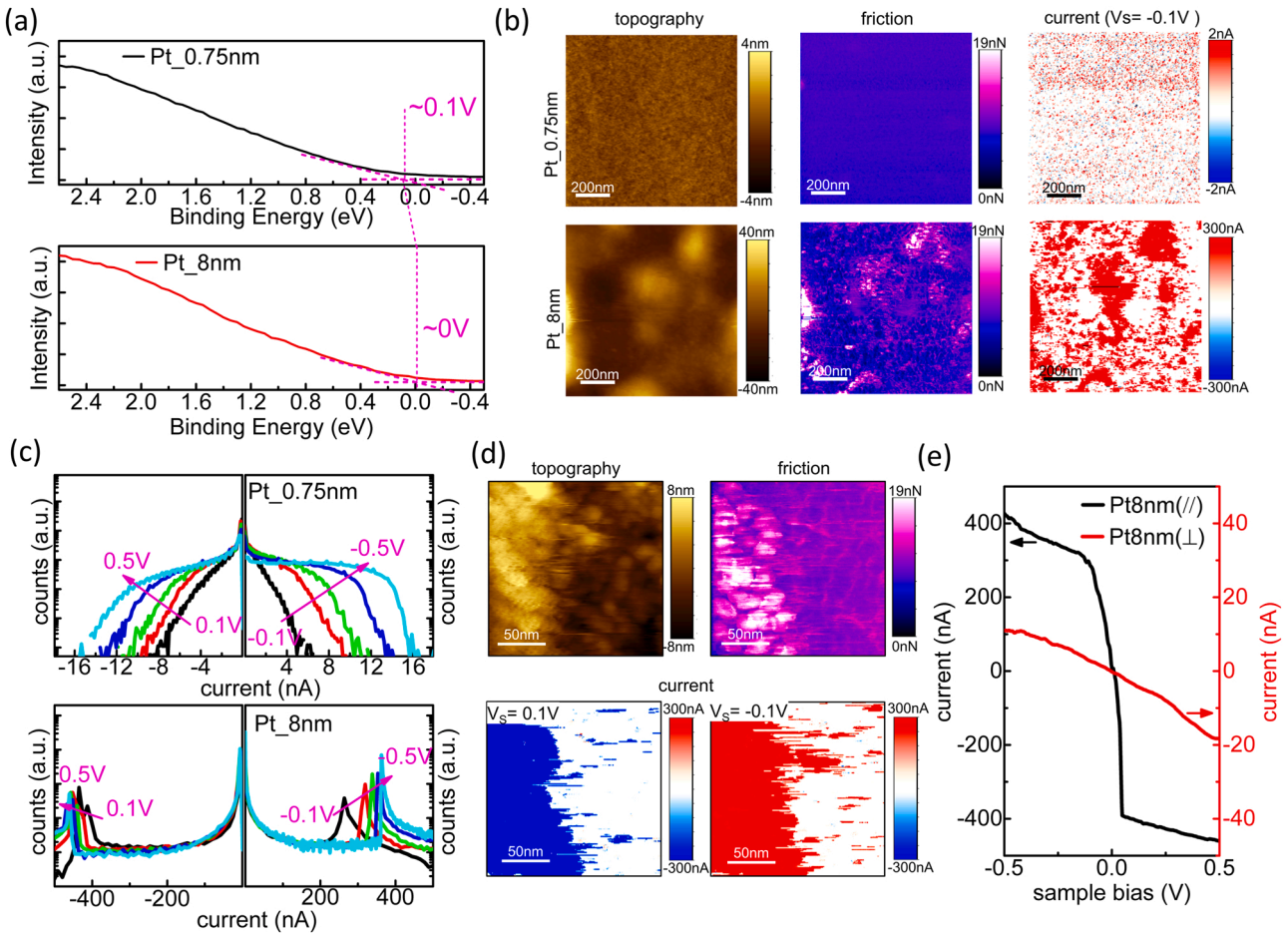

Fig. 4. (a) UPS for the valence band of Pt_0.75 nm (top) and Pt_8nm (bottom). (b) SPM topography (left), friction (middle), and current (right) images obtained for Pt_0.75 nm (upper row) and Pt_8 nm (bottom row). The sample bias is − 0.1 V. The friction contrast shows a strong positive correlation with the conductivity. (c) The current distribution evolved by varying the voltage bias of Pt_0.75 nm (top) and Pt_8 nm (bottom). (d) Topography (left upper) and the corresponding friction image (right upper) of Pt_8nm. The dramatic reversal of contrast was observed in the current images when the sample bias voltage switched from + 0.1 (left bottom) to − 0.1 V (right bottom). The current variation is more significant in Pt_8nm(⊥) with high friction rather than in Pt_8nm(//) with low friction. (e) Representative local I–V curves that were obtained for Pt_8nm(⊥) (black) and Pt_8nm(//) (red), respectively.

correspond to horizontal $PtSe_2$. Fig. S10 shows how the current configurations significantly evolved by varying the bias conditions. Their voltage-dependent current responses are compiled in Fig. 4(c). As shown in the figure, when varying the sample bias voltage within the range of ± 0.5 V, a negligible increase in the current in Pt_0.75 nm was observed with a span of ± 15 nA. The bias polarity-dependent rectifying behavior was not clear. In comparison, Pt_8nm exhibited more exotic current behavior. The available current range surged up to a few hundred nanoamperes, and high-conductance regimes (of several hundreds of nanoamperes) exhibited a narrower current distribution and more sensitive voltage responses as compared to the low-current regimes. Based on the analysis of the current configurations shown in Fig. S10, we found that such a narrow current distribution was not obtained from Pt_8nm (//) but from Pt_8nm(⊥), regardless of the voltage level or its sign. Meanwhile, the low-current regimes of Pt_8nm(⊥) exhibited very mild voltage responses, similar to what was observed for Pt_0.75 nm.

For a thorough analysis, the area of Pt_8nm (250 × 250 nm^2) was scanned (Fig. 4(d)). Compared to Pt_8nm(//) with low friction, the current on Pt_8nm(⊥) with high friction responds more sensitively to the switching of V_s from 0.1 to −0.1 V. The sharp difference of electrical features between Pt_8nm(//) and Pt_8nm(⊥) can be thoroughly examined using the local current vs. voltage (I–V) spectroscopy results, which were obtained for both Pt_8nm(//) and Pt_8nm(⊥), respectively (Fig. 4 (e)). As shown in the plot, Pt_8nm(⊥) exhibited ohmic behavior, where the current is proportional to the voltage bias, and the slope corresponding to conductance was estimated to be as high as ~3700 nA/V within the range of ± 50 mV. The reduced current slope at the high-bias regime is likely to be associated with the instrumental limit of a current preamplifier. Interestingly, Pt_8nm(//) also exhibited an ohmic response, even though the conductance slope is no more than ~30 nA/V within the same voltage range. The ratio between the slopes of Pt_8nm(//) and Pt_8nm(⊥) is as high as ~120. Such large conductance difference is qualitatively explained by the intrinsic mobility anisotropy of 2D materials [49,50]. On the region of Pt_8nm(⊥), the tip-injected carrier should be predominantly driven through in-plane transport, where the mobility is ideally limited only by intrinsic phonon vibration. However, on Pt_8nm(//), carriers must overcome the potential vdW gap using several tunneling or hopping processes so that total conductivity can be confined [51]. However, despite their conductance difference, the commonly observed ohmic features indicate that both Pt_8nm(⊥) and Pt_8nm(//) possess good electrical conductivities.

More interesting results were obtained for Pt_0.75 nm. Fig. 5(a) presents the topography of Pt_0.75 nm (80 × 80 nm^2; top), together with the corresponding current images captured at V_S = −0.1 and 0.1 V (bottom). The topography indicated that the surface is configured with nanograins at a length scale of ~20 nm. This image is consistent with previous TEM results, indicating that Pt_0.75 nm is composed of horizontally bridged $PtSe_2$ nano-islands with individually different azimuthal orientations. In addition, trench-shaped depressions were observed in the intergranular bridge regions whose apparent width was

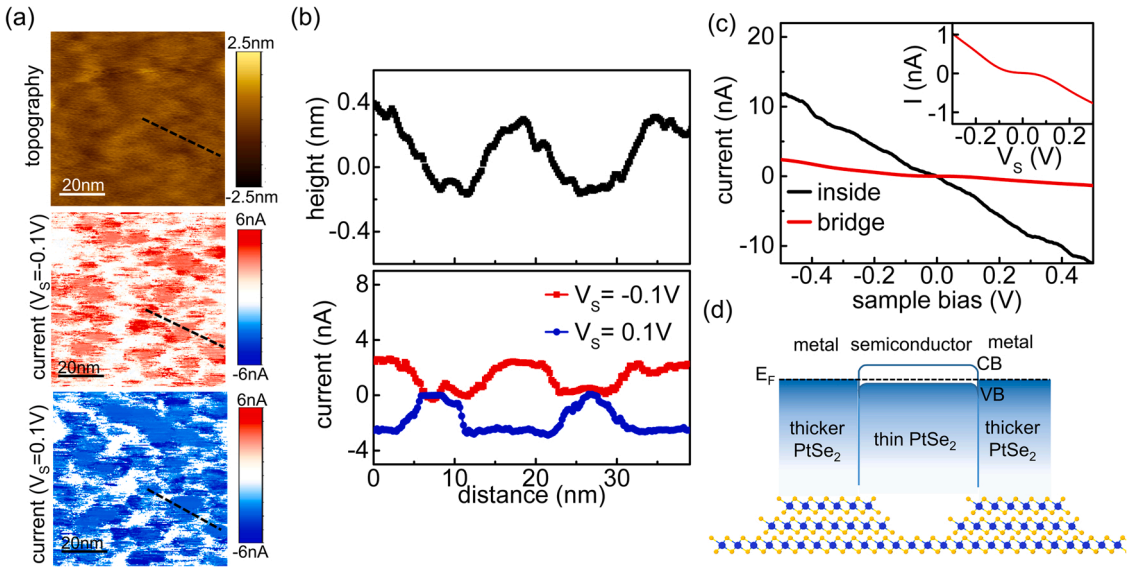

Fig. 5. (a) (top) Height images of Pt_0.75 nm, with the corresponding current images obtained at (middle) $V_s = -0.1$ V and (bottom) $V_s = +0.1$ V, respectively. (b) The cross-section profiles along the dashed lines in (a). The current level falls almost to zero when the SPM probe crosses the trench areas in topography. (c) Representative local I–V curves in the inside of grain (black) and the intergranular bridge (red). (d) Energy band diagram of $PtSe_2$ grown from ultrathin Pt film (i.e., Pt_0.75 nm). At the intergranular bridge regions, the small, but non-negligible, bandgap opening can occur owing to the thinner $PtSe_2$, which leads to the metal-semiconductor-metal junction.

approximately in the length scale of a few to ~10 nm range. The depth of the trench extended by ~0.5 or ~1 nm below the surrounding grains, which corresponds to the thickness of mono- or bi-layered $PtSe_2$. However, a more precise assessment of the shape was frequently hindered owing to the tip-sample convolution effect and the thermal drift of the scanner. By analyzing the accompanying current images, we found that the current level of bridge regions stayed near zero, even though the adjacent grain interiors exhibited a sensitive alteration of current for bias variation. To visualize the trend in detail, the representative cross-section profiles (Fig. 5(b)) were obtained from the topography and the current images along the dashed lines of Fig. 5(a). In contrast with the interior of grain, where the voltage-driven current reversal was clear, almost zero-current was obtained inside the bridged regions, regardless of switching from −0.1 to 0.1 V.

The regional conductance difference of Pt_0.75 nm can be confirmed by local I–V spectroscopy. As shown in Fig. 5(c), a noticeable difference was observed in the conductivity of the two regions. When compared with Pt_8nm(//) in Fig. 4(e), the grain interior still exhibits ohmic current behavior with comparable current range. However, in the bridge regions, the current level was depressed by nearly an order of magnitude, and a small current gap, less than ~0.2 V, emerged (inset of Fig. 4(c)), reflecting non-ohmic features [52,53]. Combined with the results of UPS (Fig. 4(a)) and a transistor device study [22], it is reasonable to ascribe the non-ohmic current behavior at the bridged region to the semiconducting property confirmed at the macroscale level. Considering the previous empirical result, that the thickness of $PtSe_2$ tends to expand by ~4 or ~5 times during the growth process relative to the Pt-seed film [22], the thicknesses of Pt_0.75 nm and Pt_8nm are in the scales of 4–5 nm and 30–40 nm, respectively. As the $PtSe_2$ layers grow, the energy level of the VBM tends to increase, because the antibonding p_z states of Se dominate the VBM [9,43]. Thus, Pt_8nm closes the bandgap, irrespective of its vertical growth length, resulting in the metallic state. However, the band energy of ultrathin and horizontal $PtSe_2$ is affected by the interlayer coupling and screening, and the monolayer- or bilayer-thinning effect at the bridge region would be discernable at Pt_0.75 nm. Fig. 5(d) shows an available growth scenario of Pt_0.75 nm, with the corresponding energy diagram where a metal-semiconductor-metal junction is formed at the bridge region with the adjacent metallic $PtSe_2$ nanograins. Therefore, the semiconducting property observed in the UPS results indicates that metal-semiconductor-metal at device scale will not completely disappear until the number of layers of $PtSe_2$ increases sufficiently. According to our previous field-effect transistor (FET) study[22], the semiconducting property would occur only when the thickness of Pt was thinner than 1 nm.

Based on the thermoelectric device, the scalable growth of $PtSe_2$ at low temperature may provide opportunities for fabricating highly efficient thermoelectric devices. To test this possibility, we fabricated a thermoelectric microdevice (Fig. S2) and measured the Seebeck coefficients of Pt_0.75 nm and Pt_8nm. The results were displayed in Fig. 6. The relatively high Seebeck coefficient of ~1150 μV/K was measured at Pt_0.75 nm, while at Pt_8nm, the coefficient decreased to ~40 μV/K. For both $PtSe_2$ samples, the positive Seebeck coefficient (p-type doping) was achieved by lowering E_F toward the valence band, which agrees with the previous FET results[22] as well. As confirmed by the previous UPS and our previous FET results, such a large Seebeck coefficient of Pt_0.75 nm

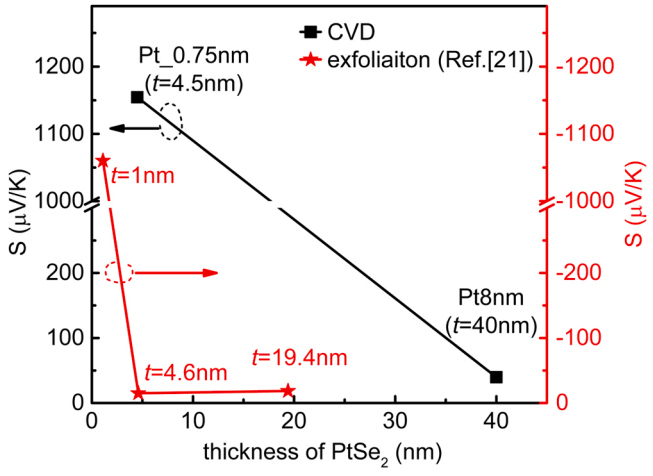

Fig. 6. Seebeck coefficient behavior of CVD-grown $PtSe_2$ (black squares). For comparison, the Seebeck coefficients obtained from exfoliated $PtSe_2$ (Ref. [21]) were plotted together (red stars).

is associated with metal-to-semiconductor transition (MST) at the thickness-modulated $PtSe_2$. The Seebeck coefficient is governed by the local density of state (DOS) near E_F; thus, the coefficient of metal tends to be small and changes little. However, in semiconductors, the closer the E_F shifts toward the edge of VBM, the greater the gradient of local DOS becomes, substantially increasing the Seebeck coefficient.[54] Especially while MST occurs, the Seebeck coefficient changes dramatically in order to reconstruct electronic structure [54,55]. Since our preceding c-AFM study clearly revealed that thickness-driven MST emerged at intergranular trench regions, we think that Seebeck coefficient of Pt_0.75 nm is dominantly impacted by MST at the thin $PtSe_2$ of the local bridge regions, where E_F could be positioned near the VBM located along *Γ-K* points [19,22]. Besides, such narrow trench structures could additionally cause the energy filtering effect [56,57] to promote the Seebeck coefficient, with virtually no harm to electron transport. If the bridge region with semiconducting property can work as an energy barrier to effectively screen the low-energy carriers (or minority carriers), Seebeck coefficient can eventually increase even more. Indeed, the high mobility of ~625 cm^2/V in our previous FET study[22] supports our assumption that the scattering effect to transport in the bridge region is still below an allowable range. However, such a local effect should become insignificant for Pt_8nm, which is entirely metallic, thereby substantially reducing the overall Seebeck coefficient. The MST-related boost-up of the Seebeck coefficient was reported from the exfoliated $PtSe_2$ with various thicknesses [21]. For comparison with our results, the Seebeck coefficient results were plotted together, as shown in Fig. 6 (red stars). In the study, bilayer $PtSe_2$ exhibited a comparably high Seebeck coefficient crossing MST. It was computed that the Seebeck coefficient of $PtSe_2$[21], like $PdSe_2$[58], would theoretically not be significantly affected by the decrease of thickness in the metallic regime. Besides, according to our recent report [22], the conductance at 0 V-gate bias monotonically decreased with thickness and the band gap energies become zero, regardless of their vertical lengths in the regime. Therefore, it is anticipated that thermoelectric power factor (defined as the product of the squared Seebeck coefficient and electrical conductivity) should be dominated by the conductivity and be reduced with the decreasing thickness before MST. However, after crossing MST, the power factor will be enhanced by Seebeck value and controlled by the gate-voltage variation. As thermoelectric performance can have an optimal thickness between the two competing effects, the exact explanation needs further investigation.

To the best of our knowledge, the role of the local MST effect present only in the scalable $PtSe_2$ has never been discussed before. Mo- or W-based TMDCs suffer from thickness-indifferent Seebeck coefficients, owing to their relatively mild band modulation with respect to thickness [59,60]; our results, based on CVD-grown $PtSe_2$, suggest that the availability of large-scaled $PtSe_2$ is promising for the future.

4. Conclusions

Although versatile properties of $PtSe_2$ pave a way for a new class of 2D devices, due to its unique correlations among thickness, structure, and other properties present potential challenges. In this study, we prepared two kinds of 2D $PtSe_2$ by controlling the thickness of Pt-seed film: (i) one with horizontal alignment and (ii) one with vertical and horizontal alignments. Based on the SPM measurement, the study on local friction showed that the friction of 2D $PtSe_2$ with different growth direction configurations exhibited distinctively different behaviors, owing to the modulus-induced contact area variation. On the other hand, the study on local conductance suggested that $PtSe_2$ with both layer directions maintains the metallic state for both growth directions, despite the significant conductance disparity. However, the sample with the horizontal alignments exhibited the semiconducting behavior in the intergranular region in contrast to the metallic grain interior. Considering electrical and thermoelectric applications, local MST of $PtSe_2$ layers in intergranular regions can severely affect the device-scale properties of $PtSe_2$. This work provides key techniques to characterize the intrinsically anisotropic features of 2D $PtSe_2$ and indicates a broad potential of $PtSe_2$ in multifunctional applications.

CRediT authorship contribution statement

Jong Hun Kim: SPM/PES/Raman-measurement and analysis, thermoelectric analysis, writing. **Seonhye Youn**: Thermoelectric measurement and analysis, writing. **Tae Won Go**: SPM-measurement and analysis. **Jeongmin Kim, and Seong-Jae Jeong**: Thermoelectric measurement and analysis. **Changhyeon Yoo and Mashiyat Sumaiya Shawkate**: sample synthesis, editing. **Sang Sub Han**: TEM characterization, editing. **Yeonwoong Junge**: Supervision, Writing – review & editing, **Jeong Young Park**: Supervision, Writing – review & editing. **Wooyoung Lee**: Supervision, reviewing.

Declaration of Competing Interest

The authors declare that they have no known competing financial interests or personal relationships that could have appeared to influence the work reported in this paper.

Acknowledgments

This work was supported by Yonsei-KIST Institutional Program of South Korea (Project No. 2Z06430-20-P069), and the Technology Innovation Program (‘20013621’, Center for Super Critical Material Industrial Technology) funded by the Ministry of Trade, Industry & Energy (MOTIE) of South Korea, and Basic Science Research Program through the National Research Foundation of Korea (NRF) funded by the Ministry of Education (NRF-2019R1A6A1A11055660) of South Korea. J.Y. Park acknowledges support from Institute for Basic Science (IBS-R004) funded by Ministry of Science, ICT and Future Planning of South Korea. Y. Jung acknowledges support from Creative Materials Discovery Program through the National Research Foundation of Korea (NRF) funded by the Ministry of Science, ICT and Future Planning (NRF-2017M3D1A1039553) of South Korea.

Appendix A. Supporting information

Supplementary data associated with this article can be found in the online version at doi:10.1016/j.nanoen.2021.106693.

References

[1] K.F. Mak, C. Lee, J. Hone, J. Shan, T.F. Heinz, Atomically thin MoS_2: a new direct-gap semiconductor, Phys. Rev. Lett. 105 (2010), 136805.
[2] S. Tongay, S.S. Varnoosfaderani, B.R. Appleton, J. Wu, A.F. Hebard, Magnetic properties of MoS_2: Existence of ferromagnetism, Appl. Phys. Lett. 101 (2012), 123105.
[3] J.H. Kim, J.H. Jeong, N. Kim, R. Joshi, G.-H. Lee, Mechanical properties of two-dimensional materials and their applications, J. Phys. D: Appl. Phys. 52 (2018), 083001.
[4] S. Manzeli, D. Ovchinnikov, D. Pasquier, O.V. Yazyev, A. Kis, 2D transition metal dichalcogenides, Nat. Rev. Mater. 2 (2017) 17033.
[5] J.Y. Park, S. Kwon, J.H. Kim, Nanomechanical and charge transport properties of two-dimensional atomic sheets, Adv. Mater. Interfaces 1 (2014), 1300089.
[6] Q.H. Wang, K. Kalantar-Zadeh, A. Kis, J.N. Coleman, M.S. Strano, Electronics and optoelectronics of two-dimensional transition metal dichalcogenides, Nat. Nanotechnol. 7 (2012) 699–712.
[7] D. Jariwala, V.K. Sangwan, L.J. Lauhon, T.J. Marks, M.C. Hersam, Emerging device applications for semiconducting two-dimensional transition metal dichalcogenides, ACS Nano 8 (2014) 1102–1120.
[8] C. Tan, H. Zhang, Two-dimensional transition metal dichalcogenide nanosheet-based composites, Chem. Soc. Rev. 44 (2015) 2713–2731.
[9] W. Zhang, J. Qin, Z. Huang, W. Zhang, The mechanism of layer number and strain dependent bandgap of 2D crystal $PtSe_2$, J. Appl. Phys. 122 (2017), 205701, 73.
[10] A. Ciarrocchi, A. Avsar, D. Ovchinnikov, A. Kis, Thickness-modulated metal-to-semiconductor transformation in a transition metal dichalcogenide, Nat. Commun. 9 (2018) 919.
[11] Y. Wang, L. Li, W. Yao, S. Song, J. Sun, J. Pan, X. Ren, C. Li, E. Okunishi, Y.-Q. Wang, Monolayer $PtSe_2$, a new semiconducting transition-metal-

dichalcogenide, epitaxially grown by direct selenization of Pt, Nano Lett. 15 (2015) 4013–4018.
[12] G. Wang, Z. Wang, N. McEvoy, P. Fan, W.J. Blau, Layered $PtSe_2$ for sensing, photonic, and (Opto-) electronic applications, Adv. Mater. 33 (2021), 2004070.
[13] H.L. Zhuang, R.G. Hennig, Computational search for single-layer transition-metal dichalcogenide photocatalysts, J. Phys. Chem. C 117 (2013) 20440–20445.
[14] W. Zhang, Z. Huang, W. Zhang, Y. Li, Two-dimensional semiconductors with possible high room temperature mobility, Nano Res. 7 (2014) 1731–1737.
[15] X.-L. Shi, W.-Y. Chen, T. Zhang, J. Zou, Z.-G. Chen, Fiber-based thermoelectrics for solid, portable, and wearable electronics, Energy Environ. Sci. 14 (2021) 729–764.
[16] M. Dargusch, W.D. Liu, Z.G. Chen, Thermoelectric generators: alternative power supply for wearable electrocardiographic systems, Adv. Sci. 7 (2020), 2001362.
[17] Y.-X. Chen, X.-L. Shi, Z.-H. Zheng, F. Li, W.-D. Liu, W.-Y. Chen, X.-R. Li, G.-X. Liang, J.-T. Luo, P. Fan, Two-dimensional WSe_2/SnSe pn junctions secure ultrahigh thermoelectric performance in n-type Pb/I Co-doped polycrystalline SnSe, Mater. Today Phys. 16 (2021), 100306.
[18] X.-L. Shi, J. Zou, Z.-G. Chen, Advanced thermoelectric design: from materials and structures to devices, Chem. Rev. 120 (2020) 7399–7515.
[19] S.-D. Guo, Biaxial strain tuned thermoelectric properties in monolayer $PtSe_2$, J. Mater. Chem. C 4 (2016) 9366–9374.
[20] H. Usui, K. Kuroki, S. Nakano, K. Kudo, M. Nohara, Pudding-mold-type band as an origin of the large seebeck coefficient coexisting with metallic conductivity in carrier-doped $FeAs_2$ and $PtSe_2$, J. Electron. Mater. 43 (2014) 1656–1661.
[21] H. Moon, J. Bang, S. Hong, G. Kim, J.W. Roh, J. Kim, W. Lee, Strong thermopower enhancement and tunable power factor via semimetal to semiconductor transition in a transition-metal dichalcogenide, ACS Nano 13 (2019) 13317–13324.
[22] S.S. Han, J.H. Kim, C. Noh, J.H. Kim, E. Ji, J. Kwon, S.M. Yu, T.-J. Ko, E. Okogbue, K.H. Oh, Horizontal-to-vertical transition of 2D layer orientation in low-temperature chemical vapor deposition-grown $PtSe_2$ and its influences on electrical properties and device applications, ACS Appl. Mater. Interfaces 11 (2019) 13598–13607.
[23] E. Okogbue, S.S. Han, T.-J. Ko, H.-S. Chung, J. Ma, M.S. Shawkat, J.H. Kim, J. H. Kim, E. Ji, K.H. Oh, Multifunctional two-dimensional $PtSe_2$-layer kirigami conductors with 2000% stretchability and metallic-to-semiconducting tunability, Nano Lett. 19 (2019) 7598–7607.
[24] M.S. Shawkat, H.-S. Chung, D. Dev, S. Das, T. Roy, Y. Jung, Two-dimensional/three-dimensional Schottky junction photovoltaic devices realized by the direct CVD growth of vdw 2D $PtSe_2$ layers on silicon, ACS Appl. Mater. Interfaces 11 (2019) 27251–27258.
[25] C.P. Green, H. Lioe, J.P. Cleveland, R. Proksch, P. Mulvaney, J.E. Sader, Normal and torsional spring constants of atomic force microscope cantilevers, Rev. Sci. Instrum. 75 (2004) 1988–1996.
[26] M. Varenberg, I. Etsion, G. Halperin, An improved wedge calibration method for lateral force in atomic force microscopy, Rev. Sci. Instrum. 74 (2003) 3362–3367.
[27] J.H. Kim, D. Fu, S. Kwon, K. Liu, J. Wu, J.Y. Park, Crossing thermal lubricity and electronic effects in friction: vanadium dioxide under the metal–insulator transition, Adv. Mater. Interfaces 3 (2016) 1500388.
[28] B.V. Derjaguin, V.M. Muller, Y.P. Toporov, Effect of contact deformations on the adhesion of particles, J. Colloid Interface Sci. 53 (1975) 314–326.
[29] J.E. Jakes, Improved methods for nanoindentation Berkovich probe calibrations using fused silica, J. Mater. Sci. 53 (2018) 4814–4827.
[30] J.H. Kim, S. Kang, J.-W. Park, E.-D. Park, Y.-K. Jun, J.Y. Han, J.H. Jung, N. Kim, G.-H. Lee, Tailored hydrogen-free carbon films by tuning the sp^2/sp^3 configuration, ACS Appl. Electron. Mater. 3 (2021) 1771–1779.
[31] H. Moon, J. Kim, J. Bang, S. Hong, S. Youn, H. Shin, J.W. Roh, W. Shim, W. Lee, Semimetallic features in thermoelectric transport properties of 2H–3R phase niobium diselenide, Nano Energy 78 (2020), 105197.
[32] M. O'Brien, N. McEvoy, C. Motta, J.-Y. Zheng, N.C. Berner, J. Kotakoski, K. Elibol, T.J. Pennycook, J.C. Meyer, C. Yim, Raman characterization of platinum diselenide thin films, 2D Mater. 3 (2016), 021004.
[33] A. Shaji, K. Vegso, M. Sojkova, M. Hulman, P. Nadazdy, P. Hutar, L. Pribusova Slusna, J. Hrda, M. Bodik, M. Hodas, Orientation of few-layer MoS_2 films: in-situ x-ray scattering study during sulfurization, J. Phys. Chem. C 125 (2021) 9461–9468.
[34] J. Zhou, X. Kong, M.C. Sekhar, J. Lin, F. Le Goualher, R. Xu, X. Wang, Y. Chen, Y. Zhou, C. Zhu, Epitaxial synthesis of monolayer $PtSe_2$ single crystal on $MoSe_2$ with strong interlayer coupling, ACS Nano 13 (2019) 10929–10938.
[35] L. Fei, S. Lei, W.-B. Zhang, W. Lu, Z. Lin, C.H. Lam, Y. Chai, Y. Wang, Direct TEM observations of growth mechanisms of two-dimensional MoS_2 flakes, Nat. Commun. 7 (2016) 1–7.
[36] J.Y. Park, M. Salmeron, Fundamental aspects of energy dissipation in friction, Chem. Rev. 114 (2014) 677–711.
[37] S. Kwon, J.-H. Ko, K.-J. Jeon, Y.-H. Kim, J.Y. Park, Enhanced nanoscale friction on fluorinated graphene, Nano Lett. 12 (2012) 6043–6048.
[38] L. Xu, T.-B. Ma, Y.-Z. Hu, H. Wang, Vanishing stick–slip friction in few-layer graphenes: the thickness effect, Nanotechnology 22 (2011), 285708.
[39] X. Zeng, Y. Peng, H. Lang, L. Liu, Controllable nanotribological properties of graphene nanosheets, Sci. Rep. 7 (2017) 1–13.
[40] P. Gong, Z. Ye, L. Yuan, P. Egberts, Evaluation of wetting transparency and surface energy of pristine and aged graphene through nanoscale friction, Carbon 132 (2018) 749–759.
[41] X. Zeng, Y. Peng, M. Yu, H. Lang, Xa Cao, K. Zou, Dynamic sliding enhancement on the friction and adhesion of graphene, graphene oxide, and fluorinated graphene, ACS Appl. Mater. Interfaces 10 (2018) 8214–8224.
[42] R.A. Soler-Crespo, W. Gao, L. Mao, H.T. Nguyen, M.R. Roenbeck, J.T. Paci, J. Huang, S.T. Nguyen, H.D. Espinosa, The role of water in mediating interfacial adhesion and shear strength in graphene oxide, ACS Nano 12 (2018) 6089–6099.
[43] Y. Zhao, J. Qiao, Z. Yu, P. Yu, K. Xu, S.P. Lau, W. Zhou, Z. Liu, X. Wang, W. Ji, High-electron-mobility and air-stable 2D layered $PtSe_2$ FETs, Adv. Mater. 29 (2017), 1604230.
[44] H. Zhang, Z. Guo, H. Gao, T. Chang, Stiffness-dependent interlayer friction of graphene, Carbon 94 (2015) 60–66.
[45] E. Riedo, H. Brune, Young modulus dependence of nanoscopic friction coefficient in hard coatings, Appl. Phys. Lett. 83 (2003) 1986–1988.
[46] L. Fang, D.-M. Liu, Y. Guo, Z.-M. Liao, J.-B. Luo, S.-Z. Wen, Thickness dependent friction on few-layer MoS_2, WS_2, and WSe_2, Nanotechnology 28 (2017), 245703.
[47] C. Lee, Q. Li, W. Kalb, X.-Z. Liu, H. Berger, R.W. Carpick, J. Hone, Frictional characteristics of atomically thin sheets, Science 328 (2010) 76–80.
[48] J.H. Kim, C. Hyun, H. Kim, J.K. Dash, K. Ihm, G.-H. Lee, Thickness-insensitive properties of α-MoO_3 nanosheets by weak interlayer coupling, Nano Lett. 19 (2019) 8868–8876.
[49] K.-K. Kam, Electrical properties of WSe2, WS2, MoSe2, MoS2, and their use as photoanodes in a semiconductor liquid junction solar cell, DOI (1982). (Ph.D. Thesis).
[50] B. Evans, P. Young, Optical absorption and dispersion in molybdenum disulphide, Proc. R. Soc. Lond. Ser. A: Math. Phys. Sci. 284 (1965) 402–422.
[51] S. Najmaei, M.R. Neupane, B.M. Nichols, R.A. Burke, A.L. Mazzoni, M.L. Chin, D. A. Rhodes, L. Balicas, A.D. Franklin, M. Dubey, Cross-plane carrier transport in van der waals layered materials, Small 14 (2018), 1703808.
[52] S. Kwon, S.J. Lee, S.M. Kim, Y. Lee, H. Song, J.Y. Park, Probing the nanoscale Schottky barrier of metal/semiconductor interfaces of Pt/CdSe/Pt nanodumbbells by conductive-probe atomic force microscopy, Nanoscale 7 (2015) 12297–12301.
[53] K. Szot, W. Speier, G. Bihlmayer, R. Waser, Switching the electrical resistance of individual dislocations in single-crystalline $SrTiO_3$, Nat. Mater. 5 (2006) 312–320.
[54] T. Katase, K. Endo, H. Ohta, Thermopower analysis of metal-insulator transition temperature modulations in vanadium dioxide thin films with lattice distortion, Phys. Rev. B 92 (2015), 035302.
[55] A. Bentien, S. Johnsen, G. Madsen, B. Iversen, F. Steglich, Colossal Seebeck coefficient in strongly correlated semiconductor $FeSb_2$, EPL Europhys. Lett. 80 (2007) 17008.
[56] C. Gayner, Y. Amouyal, Energy filtering of charge carriers: current trends, challenges, and prospects for thermoelectric materials, Adv. Funct. Mater. 30 (2020), 1901789.
[57] Y. Lin, M. Wood, K. Imasato, J.J. Kuo, D. Lam, A.N. Mortazavi, T.J. Slade, S. A. Hodge, K. Xi, M.G. Kanatzidis, Expression of interfacial Seebeck coefficient through grain boundary engineering with multi-layer graphene nanoplatelets, Energy Environ. Sci. 13 (2020) 4114–4121.
[58] Y. Zhao, P. Yu, G. Zhang, M. Sun, D. Chi, K. Hippalgaonkar, J.T. Thong, J. Wu, Low-symmetry $PdSe_2$ for high performance thermoelectric applications, Adv. Funct. Mater. 30 (2020), 2004896.
[59] J. Hong, C. Lee, J.-S. Park, J.H. Shim, Control of valley degeneracy in MoS_2 by layer thickness and electric field and its effect on thermoelectric properties, Phys. Rev. B 93 (2016), 035445.
[60] D. Wickramaratne, F. Zahid, R.K. Lake, Electronic and thermoelectric properties of few-layer transition metal dichalcogenides, J. Chem. Phys. 140 (2014), 124710.

Jong Hun Kim is a research professor in Department of Materials Science and Engineering at Yonsei University. He earned his Ph.D. in Physics with scanning probe microscopy related study on local electrical properties of thin dielectric materials at Seoul National University. He is currently a research professor of Department of Materials Science and Engineering at Yonsei University. His research interests focus on exploring the structural, electronic, thermal, and mechanical phenomena on low dimensional materials through the scanning probe microscopies and other advanced surface characterization techniques.

Seonhye Youn received a Bachelor's degree in chemical Engineering from Kongju National University in 2016. she is currently M.S candidate at the Department of Materials Science and Engineering in Yonsei University under the supervision of Prof. Wooyoung Lee. She is currently studying on the nano thermoelectric materials.

Tae Won Go received his Master's Degree in 2018 from Department of Materials Science and Engineering at Seoul National University. He is currently a doctoral candidate under Professor Jeong Young Park at Department of Chemistry, Korea Advanced Institute of Science and Technology (KAIST). His main research interests focus on investigating the tribological properties of confined water intercalated between graphene and hydrophilic surfaces by friction force microscopy (FFM) technique.

Jeongmin Kim is a senior researcher of the Division of Nanotechnology at DGIST in Korea. He obtained his B.S. degree in metallurgical engineering from Yonsei University in Korea. After receiving his Ph.D. degree in material science and engineering at Yonsei University, he worked as a postdoctoral researcher at UC San Diego and a research professor at Yonsei University. Throughout this time, his prime focus of research has been on 1D and 2D structures to study and enhance the material properties for applications as sensors and energy materials.

Changhyeon Yoo received a Bachelor's degree in Physics from Seoul National University in 2003. After his Ph.D. Degree in Physics at the University of North Dakota, he is currently a Post-doctoral Associate at the NanoScience Technology Center at the University of Central Florida under the supervision of Prof. Yeonwoong Jung. He is currently focused on the investigation of the 2D materials: Layered transition metal dichalcogenides.

Mashiyat Sumaiya Shawkat obtained a Bachelor's degree in Electrical and Electronic Engineering from BRAC University in 2014. She is currently pursuing a Ph.D. degree at the University of Central Florida, majoring in Electrical Engineering. Her research is focused on two-dimensional materials synthesis; and application in novel electronic and optoelectronic devices.

Sang Sub Han obtained a Bachelor's degree in Materials Science and Engineering from Hanyang University in 2012, and Ph.D. degree of materials Science and Engineering from Seoul National Univerisy in 2021. He is currently a Post-doctoral associate at the University of Central Florida. His research is focused on the inverstigation of the two dimensional mateirlas; synthesis and transfer for the future electrocnic devices.

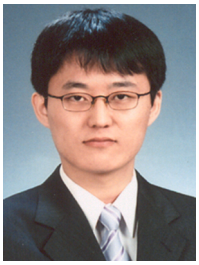

Seong-jae Jeon received his Ph.D. degree in Advanced Materials Science and Engineering from Sungkyunkwan University Republic of Korea. His research interests are mainly focused on thin film and bulk thermoelectric materials, devices, modules and their systems for Energy harvesting and Cooling.

Yeonwoong Jung is an assistant professor in the department of Materials Science & Engineering with joint appointments in NanoScience & Technology Center and Electrical & Computer Engineering of the University of Central Florida. Jung has a bachelor's degree in materials science and engineering from Seoul National University, a master's degree from the University of Illinois, Urbana-Champaign, and a doctorate from the University of Pennsylvania. He has also served as a visiting scholar for the Los Alamos National Laboratory in New Mexico; and a post-doctoral scholar at Yale University. His research explores low dimensional materials including 2D atomic layers for transformative technologies in energy, environmental, and electronic applications.

Jeong Young Park currently is a professor at Department of Chemistry, Korea Advanced Institute of Science and Technology, and an associate director of Center for Nanomaterials and Chemical Reactions, Institute for Basic Science, Republic of Korea. He received his Ph.D. from Seoul National University in 1999, followed by the work as a staff scientist at Lawrence Berkeley National Laboratory. His research focuses on surface phenomena covering energy dissipation and conversion at surfaces, nanotribology, catalysis, and renewable energy conversion. He has published 310 peer-reviewed articles and book chapters in the fields of surface science and catalysis.

Wooyoung Lee is a professor of the Department of Materials Science and Engineering and the Director of the Center for Super Critical Material Industrial Technology (MOTIE) at Yonsei University in Korea. He received a Ph.D. degree in physics from the University of Cambridge, United Kingdom, in 2000. He is a regular member of the National Academy of Engineering of Korea. His research interests have centered on hydrogen sensors, various metal oxide semiconducting gas sensors, and thermoelectric materials and devices.